Acta Montanistica Slovaca
ISSN 1335-1788
actamont.tuke.sk

Geophysical exploration of tungsten–copper deposit using the wide-field electromagnetic method

Xiaoli XIE[1], Shujing JIA[1], Yan ZENG[1], Tianyu ZHANG[2], Chunlei GE[1], Siliu YU[1] and Jie ZHU[3]

Authors' affiliations and addresses:
[1] School of Civil Engineering, Guangxi Polytechnic of Construction, Nanning, Guangxi, China

[2] School of Mechanical Engineering, Jiangsu University of Technology, Changzhou, Jiangsu, China

[3] Civil-Military Integration Center, China Geological Survey, Chengdu, Sichuan, China

***Correspondence:**
Chunlei GE, School of Civil Engineering, Guangxi Polytechnic of Construction, Nanning, Guangxi, China
e-mail: 13907811569@163.com

Siliu YU, School of Civil Engineering, Guangxi Polytechnic of Construction, Nanning, Guangxi, China
e-mail: siliuyu@163.com

How to cite this article:
Xie, X., Jia, S., Zeng, Y., Zhang, T., Ge, C., Yu, S. and Zhu, J. (2024). Geophysical exploration of tungsten–copper deposit using the wide-field electromagnetic method. *Acta Montanistica Slovaca*, Volume 29 (3), 724-739

DOI:
https://doi.org/10.46544/AMS.v29i3.18

Abstract
The Zhuxi tungsten–copper (W–Cu) deposit is a large skarn-type deposit. The buried depth of the primary ore body exceeds 1000 m, and the occurrence of the primary ore-controlling structure is unknown, highlighting the need for deep exploration. In this study, a wide-field electromagnetic method (WFEM) was applied for deep W–Cu mine detection in the Zhuxi mining area. The relationships among the target body's electrical properties, density, magnetism, and lithology were established using physical property data and a drill-resistivity sounding curve. Combined with known geological data, a two-dimensional geological–geophysical section was drawn, and a three-dimensional geological prospecting model was established based on the inversion of a three-dimensional section slice map of the WFEM. The results show that the WFEM can reveal the distribution pattern of the primary ore-bearing structure and horizon in this area. In addition, hydrothermal alteration activity related to deeply buried rock masses can be obtained, providing a strong basis for the study of metallogenic regularity at a 500–3000 m depth in the Zhuxi mining area and the prognosis for further prospecting.

Keywords
Zhuxi mining region; Tungsten–copper deposits; Wide field electromagnetic method; Skarn; Geophysical exploration.

Introduction

The Zhuxi tungsten–copper (W–Cu) polymetallic mining area is located at China's eastern end of the Qin–Hang junction zone (Yang and Mei 1997). The discovery of the mine altered the perception of the resource distribution pattern in Jiangxi Province as "south tungsten and north copper" and introduced the concept of prospecting for large deposits in the Taqian–Fuchun ore concentration area (Wu et al., 2015; Wei, 2016). During the blind depth exploration stage (2010–2019), the controlled extension along the strike of the concealed ore body in the Zhuxi area was > 1800 m, whereas the controlled extension along the dip was nearly 2000 m, and neither the strike nor the dip of the primary ore body was controlled to the boundary (Chen et al., 2012; Wang, 2020). Many studies have been conducted focusing on the geological characteristics and ore-controlling conditions (Chen, 2014; Ouyang et al., 2014; Chen et al., 2015; Wang et al., 2021), diagenesis and ore-forming age (Li et al., 2014; Liu et al., 2014; Wan et al., 2015; He et al., 2018), metallogenic regularity, and prospecting direction of the Zhuxi W–Cu deposit and have explored and formulated the Zhuxi-type vein surface body prospecting method (Liu et al., 2015; Xia and Wang, 2016; Ouyang et al., 2018; Ouyang et al., 2019). By understanding key ore-forming elements such as ore-control in the thrust (slip) overburden fault zone, mineralisation in carbonate tectonic slabs, and ore-formation in the Yanshanian granite mass (Xie et al., 2015), we achieved a major prospecting breakthrough by "finding the body by veins", "finding the body by layers", and "pursuing the body by surfaces" (He et al., 2011).

The formation of a deep rock mass in the Zhuxi W-Cu deposit is considered to be related to hydrothermal alteration activity, which is one of the primary points of discussion in this study. This feature of the W-Cu deposit in the study area differs from that in other regions of the world. Porphyry-type Cu(-Au) deposits primarily occur in the continental margins and island magmatic arcs, whereas porphyry-type molybdenum (Mo) deposits occur in continental margin back-arc extensional zones (Mao et al., 2011; Richards, 2011). However, the granite-related deposits are not restricted to a particular tectonic setting. For example, granite-related mineralisation of W, tin (Sn), and tantalum (Ta) may form in several different tectonic settings (Mao et al., 2019). As the mineralisation of different ore elements involves different magma sources, there is a systematic (although overlapping) relationship between the oxygen fugacity of the intrusion and the enriched ore elements. The involvement of mantle-derived melts results in oxidised systems as found in Cu and Mo deposits, whereas the melting of sedimentary rocks results in reduced systems as found in Sn, lithium (Li), and Ta deposits (Candela and Bouton, 1990; Cerný et al., 2005). Tungsten is unusual because it may form deposits in both reduced (W-Sn-F) and oxidised (W-Mo-Cu) granitic intrusions (Meinert et al., 2005). The nature of the source materials and their redox states play an important role in determining the elements that are efficiently mobilised during partial melting (Hart et al., 2004). The redox state of the magma also influences which elements are concentrated during magmatic fractionation and which elements are scavenged by silicate and oxide minerals and are thus depleted rather than enriched (Jugo, 2009). Fractional crystallisation of the magma results not only in the enrichment of ore elements but also in the enrichment of volatile elements, which eventually leads to the separation of the fluid phase (Annen et al., 2006). The partitioning behaviour of ore elements between the melt and fluid states determines whether the economic concentrations of ore elements will be bound to magmatic minerals in the intrusion or hydrothermal minerals within the intrusion or its wall rocks (Mengason et al. 2011; Schmidt et al. 2020).

Geophysical and geochemical techniques play an important role in the surface and point prospecting stages in the Zhuxi mining area. Regarding the mining area scale, (Yan, 2017) conducted research on a quality geophysical profile, obtained information on the deep magnetic source and low-density hidden rock mass through gravity, magnetic, and CSAMT, and constructed a prospecting model that included polarisation and resistivity anomalies. (Zhang et al., 2018) used low-flying aeromagnetic technology to classify eight deep faults and suggested four potential metallogenic areas. Based on 1:50,000 gravity and aeromagnetic data, (Guo et al., 2020) established a peripheral structural framework and a three-dimensional geological–geophysical model of the Zhuxi area using gravity and magnetic three-dimensional inversion modelling. They conducted a three-dimensional identification of the buried rock mass. However, with deep exploration required in the Zhuxi mining area, it is difficult to satisfy "point" deep exploration requirements, such as greater burial depth, smaller scale, and complex geological conditions, by relying only on traditional geophysical exploration methods.

He (2010(a)) proposed the wide-field electromagnetic method (WFEM), which is highly relevant to geophysical communities. This method adopts technologies such as high-power transmission and the transmission and reception of wideband spectrum signals, which greatly improves the frequency data density and signal-to-noise ratio and has the advantages of high efficiency, strong anti-interference ability, and high measurement accuracy, realising a leap from extensive to accurate electromagnetic analysis (He, 2010(b); He, 2019). The WFEM has a significant ability to penetrate deep geological structures.

Some scholars have conducted related research on WFEM data processing. (Li et al., 2021) proposed a WFEM denoising method based on a combination of velocity Fourier transform, complementary global empirical mode decomposition, and shift-invariant sparse coding to remove accurately power–frequency interference, correct baseline drift, sparse representation, and dictionary learning to eliminate strong interference

in signals and reconstruct high-quality pseudo-random useful signals. The obtained apparent resistivity and electric field curves were stable and continuous. (Ling et al., 2022) proposed a method for extracting high-frequency effective information based on time-signal reconstruction, recording the time series of transmitted and received signals, estimating crystal vibrational errors through time series for correction and reconstruction, extracting high-frequency effective information, suppressing the upwarp phenomenon of the high-frequency section, and obtaining accurate high-frequency components. The above method can denoise the collected time-domain data, improve data quality, and achieve satisfactory results in practical applications.

In this study, a wide-area electromagnetic deep exploration experiment was conducted in the Zhuxi area, focusing on deep structural characterisation "at a certain point". Guided by the "vein surface body" prospecting method, the experimental process of detecting W–Cu ore in Zhuxi using the WFEM is systematically described, including the data processing, qualitative analysis, inversion interpretation, electrical information extraction, and comprehensive geological–geophysical interpretation procedures. From the perspective of electrical structures, the understanding of super-large Cu polymetallic deposits has deepened, and the validity of applying WFEM to deep metal mineral prospecting has been verified.

Geological Setting

Geological conditions. The research area is located in Fuliang County, Jiangxi Province, China (Fig. 1(a)), and the layout of the WFEM lines is shown in Fig. 1(b). The strata in this area developed in the Neoproterozoic (Pt3), Carboniferous to Triassic (C–T), Cretaceous, and Quaternary (Q), and were primarily composed of shallow metamorphic and sedimentary rocks, and a small amount of loose sediments (Fig. 1(c)) (Ouyang et al., 2023).

The basement strata in the study area are Neoproterozoic millennium deposits ($Pt_3^{1a}W$), which are primarily shallow metamorphic rocks composed of sericite, tuffaceous, and sandy phyllite, and metamorphic siltstone and sandstone. The cap rocks are primarily C–T carbonate rocks with clastic rocks and are distributed in a monoclinic structure with a NE, NW dip and dip angle of 22–86° overlying Neoproterozoic shallow metamorphic rocks in an angular unconformity. The Carboniferous Huanglong Formation (C_2h) and Chuanshan Formation (C_2c) carbonate strata were important material bases for the deposit formation and belong to the primary ore-bearing strata. The Permian system in this area is primarily distributed from bottom to top and includes the Qixia (P_2q), Maokou (P_2m), Leping (P_3l), and Changxing (P_3c) Formations. The Triassic emerged primarily from the Anyuan Group (T_3a).

Multilayer thrust (slip) overburden activity occurred in the area, causing the Neoproterozoic shallow metamorphic rock to overburden the ore body. The basement is dominated by closed folds and mesh-like shear fractures. Many fault structures were observed in the mine area, which can be divided into four groups according to the fault trend: NE-, EW-, NNE-, and NW-trending. The NE-trending faults are the most numerous, and fault F2 is closely related to mineralisation. The F1 and F2 faults are regional thrust (slip) overlying faults. The faults trend toward the NW, the dip angle changes significantly, and local inversion occurs. The upper wall of fault F1 belongs to the Neoproterozoic Wannian Group, and the lower wall belongs to the C–T system. The fault strikes 50–60° NE with a dip angle of 60–80°. Fault F2 extends 45–60° NE in a soothing wave shape and bends NW. The dip angle of fault F2 is steeper in the shallow section and gentler in the deeper section. The interlayer slippage and expansion spaces are the primary ore-hosting sites, the most important ore-controlling structures in the area, serving as magma intrusion and ore-forming fluid migration channels and the site of mineral precipitation.

Physical characteristics. Physical characteristics are the links between geophysical data and geological information, with physical data being the primary constraint for qualitative interpretation and quantitative inversion. Some scholars have qualitatively interpreted the geological information in the study area. For example, (Wang et al., 2023) analysed the ore-forming characteristics of the Zhuxi mining area and summarised the ore-forming rules. (Wei et al., 2023) studied the mineral types, associations, and other mineralogical characteristics of the Zhuxi W–Cu deposit. These scholars analysed the ore deposit information in the study area from the aspects of ore-forming location, time, and mineral composition but did not discuss the distribution form, scale, and depth of ore-controlling structures in the area.

In this study, the quantitative inversion of geophysical data was primarily conducted by combining stratigraphic lithology and physical property data in the study area. The primary geophysical inferences and interpretation markers of geological bodies can provide a basis for the interpretation of subsequent anomalous bodies and the construction of geological–geophysical models.

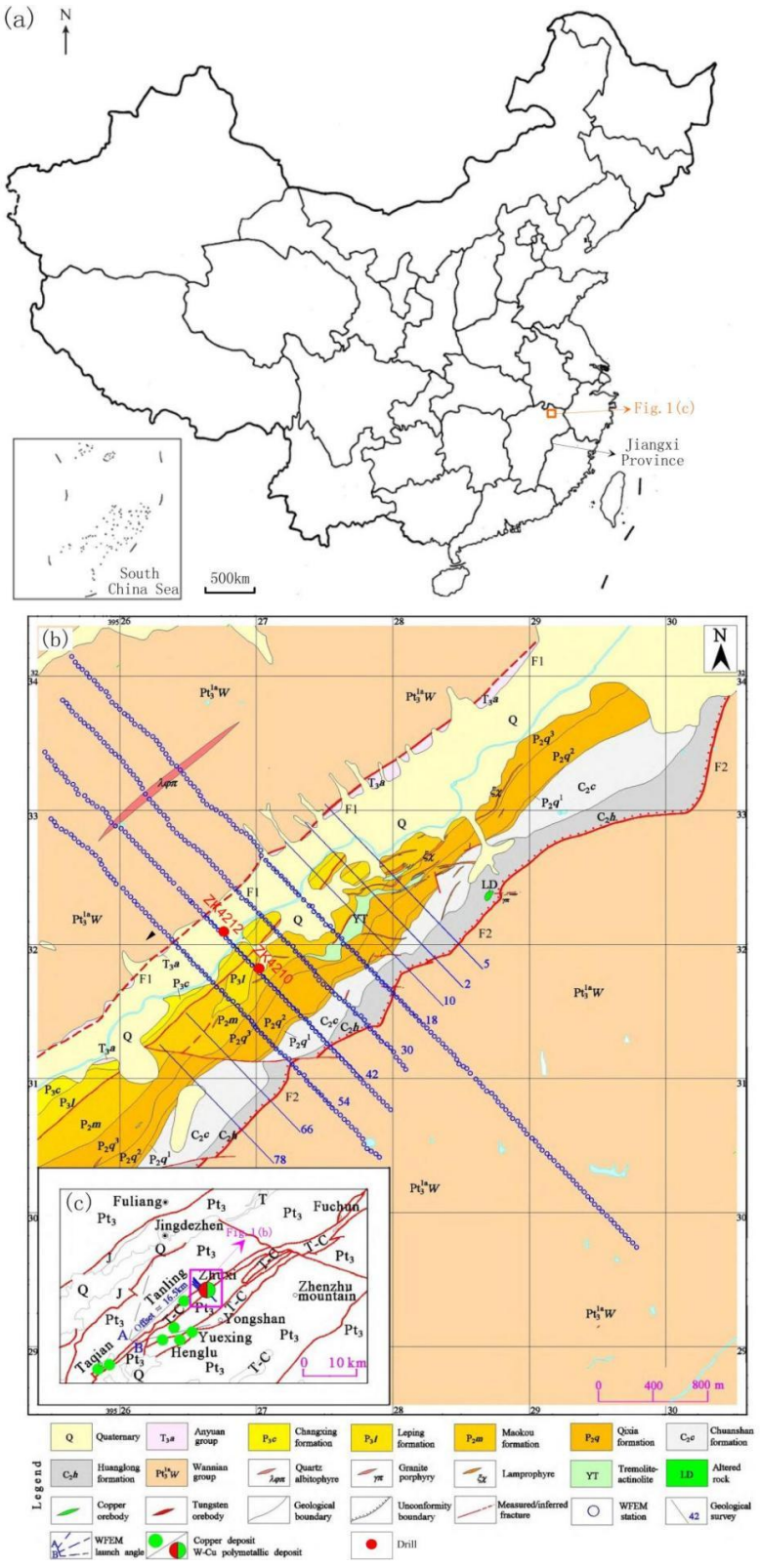

Fig. 1 Study area geological map and WFEM survey grid. (a) Study area location; (b) WFEM survey line layout; and (c) study area geological map.

The physical parameters of rocks are the primary references for studying their physical characteristics. Gravity and magnetic geophysical surveys were conducted in the study area. For example, Yan (2017) obtained deep magnetic sources and low-density rock mass information through gravity, magnetism, and CSAMT. (Zhang et al., 2018) used low-altitude aeromagnetic technology to classify eight deep faults. (Guo et al., 2020) conducted a 1:50,000 gravity–aeromagnetic survey. The physical parameters of the rock and ore used in this

study were derived from the results of these researchers. In the study area, the skarn magnetic characteristics are the highest, phyllite is weakly magnetic, and other strata are nonmagnetic; therefore, magnetic anomalies can be used to identify mineralisation alteration. The T_3a and P_3l densities were the lowest, whereas those of the other formations were approximately 2.7 g/cm^3. Skarn and marble had the highest densities, which caused a high local gravity anomaly. The average density of granite is 2.6 g/cm^3, which is approximately 0.1 g/cm^3 less than that in the surrounding rock strata, causing a local gravity anomaly. Skarn had the highest polarisability, followed by carbonaceous limestone, whereas the other strata were characterised by low polarisability. From a lithological perspective, the resistivity of limestone, dolomite, marble, and phyllite is high, that of siltstone and quartz sandstone is low, and that of limestone is reduced by hydrothermal replacement to form skarn. Marble is nonmagnetic with high density, resistivity and low polarisation, whereas skarn is characterised by high magnetism and density, low resistivity, and high polarisation. The average resistivity of granite is 2688.1 Ω·m; the surrounding rock of the deep hidden rock mass is primarily phyllite, Carboniferous limestone, and dolomite, and their resistivity is > 35,000 Ω·m (Yan, 2017). Deep rock strains and dikes are small and fragmented, are often surrounded by thick mineralisation alteration zones, and show medium and low resistivity. Therefore, it is difficult to identify and delineate rock masses using electrical data alone (Liu et al., 2018). The resistivity of P_2q_2 carbonaceous limestone varies with the amount of carbon available, with limestone characterised as a layer with relatively low resistivity between the upper and lower high resistivity layers. Such a layer can be labelled as a "low-resistivity marker layer" for the processing and interpretation of WFEM data in this area.

In summary, the physical properties of the rocks (ores) in this area differ, providing a geophysical premise for a comprehensive multiparameter study.

Methods and results

Survey **line layout.** WFEM is an artificial source-frequency domain method that uses a 2n sequence pseudo-random transmitting signal. This method uses a horizontal current as the field source and obtains wide-frequency apparent resistivity by measuring a certain component of the electromagnetic field. The observational device is shown in Fig. 2.

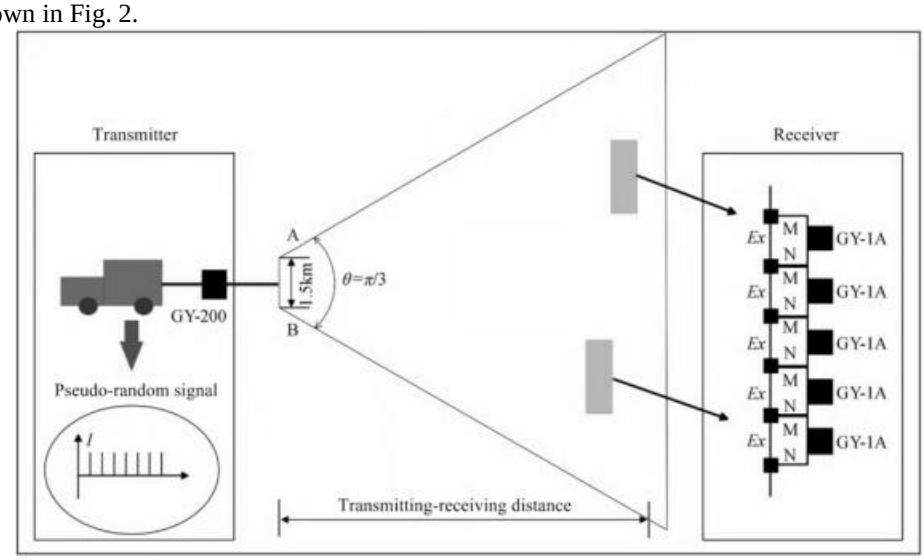

Fig. 2 Schematic diagram of the WFEM observational device.

The WFEM was mainly used to explore the "second prospecting space" at a depth of 500 – 3000 m in this area. Four WFEM survey lines coincident with the geological profiles were deployed, and the survey parameter was the horizontal component **Ex** of the electric field **E**. The four survey lines were arranged in the NE direction (Fig. 1(b) and Tab. 1).

Table 1 Survey parameters

Survey line No.	*Azimuth angle/ (°)*	*Length/ km*	*Offset/ km*	*Line spacing/ m*	*Station distance/m*	*Frequency range/ Hz*
54	*136*	*3.4*	*16.5*	*300*	*40*	*0.0117-8192 (61 frequencies)*
42		*3.7*				
30		*3.7*				
18		*6.0*				

Data processing. Obtaining reliable data is the foundation of successful geophysical exploration, and reliable inferences and interpretations are the keys to success. Data processing in the WFEM primarily involved the use of an integrated geophysical data processing and interpretation system (GME-3DI) developed by Professor He Jishan (He, 2020).

First, raw data were carefully preprocessed, the electric field was statistically corrected, and the apparent resistivity of a wide area was calculated iteratively. Subsequently, the transverse segmentation and longitudinal stratification characteristics of the electrical structure were qualitatively analysed (transverse segmentation refers to the transversal block portion on the apparent resistivity profile, whereas longitudinal stratification refers to the longitudinally layered distribution of apparent resistivity), and the inversion parameters were continuously optimised by comparing the known geological profiles, rock physical properties, and WFEM curves with those of the drills (ZK4210 and ZK4212). Finally, the 1D inversion results with field sources were used as an initial model to perform a 2.5D continuum inversion (Dai et al., 2013). During data processing, existing geological, drilling, geophysical, and other data were combined, and the model was gradually revised several times to reduce the inversion fitting error and obtain a multi-solution inversion interpretation.

Fig. 3 shows a schematic representation of the RMS inversion data. After eight iterations, the RMS of the data was < 0.2.

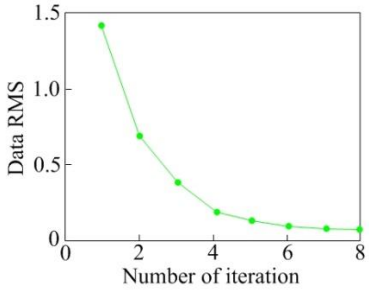

Fig. 3 Data RMS

Qualitative analysis. The characterisation of anomalous bodies is important for geophysical data interpretation. The four test sections are arranged in parallel, perpendicular to the NE direction. The corresponding stratigraphic structural units are the same, and the distribution characteristics of the underground electrical properties reflect good similarity. This study considers Survey Line 42 as an example to illustrate the qualitative analysis.

As shown in Fig. 2, the apparent resistivity of the central carboniferous Permian strata decreases (Fig. 2(a)), and the apparent resistivity curve of equal frequency (Fig. 2(c)) describes a two-level "V"-shaped structure, reflecting the characteristics of the upper and lower ore-forming steps of the silica – calcium plane (including the interface of carboniferous Permian strata and F2 fault structure) in the depth of the area. The lower metallogenic stage was the storage location of the thick and large skarn-type tungsten ore bodies. The type of curve (Fig. 2(b)) is mainly the "HKH" type, with large lateral fluctuations, which is consistent with the lithology and structure of the carboniferous Permian strata.

The apparent resistivity of the shallow metamorphic rock basement on both sides of $Pt_3^{1a}W$ increased, and the apparent resistivity curve at equal frequencies was flat. The curve was of a single type and transverse continuity, primarily the "H" type, and the front branch of the curve was short, which is presumed to be caused by factors such as shallow weathering and water, forming a high background field in the region.

The constant-frequency apparent resistivity (ρ_s) curve (Fig. 4(c)) shows that faults F1 and F2 are located on either side of the "V" structure. The variation in the apparent resistivity gradient near fault F1 was steeper, indicating that the occurrence of fault F1 was steeper. The apparent resistivity near fault F2 showed a wide and slow step change, indicating that its occurrence exhibited steep and gradual changes with depth. The flat section of fault F2 (second step) is an important deposit site in this area, with mineralisation alteration developing on both sides. The distortion and fluctuation of the apparent resistivity curves at the same frequency near the basement areas of faults F1 and F2 indicate the development of sub-basement structures of shallow metamorphic rocks on both sides and the possibility of rock mass emplacement.

Figs. 5 and 6 show the sounding curves of drills ZK4210 and ZK4212, respectively, on Survey Line 42 (the locations of drills ZK4210 and ZK4212 are shown in Fig. 1). By comparing the stratigraphic column chart and calibrating each electrical layer by constantly adjusting the inversion parameters, the obtained WFEM 1D inversion data reflect satisfactory stratification ability. P_2q_2 formation and tungsten-rich mineralised bodies often correspond to the low-resistivity layer of the HKH-type curve. The P_2m, C_2c, and C_2h carbonate strata and skarn correspond to the medium-resistivity layer, and the shallow $Pt_3^{1a}W$ metamorphic rock basement at the bottom is responsible for the deep, high-resistivity background.

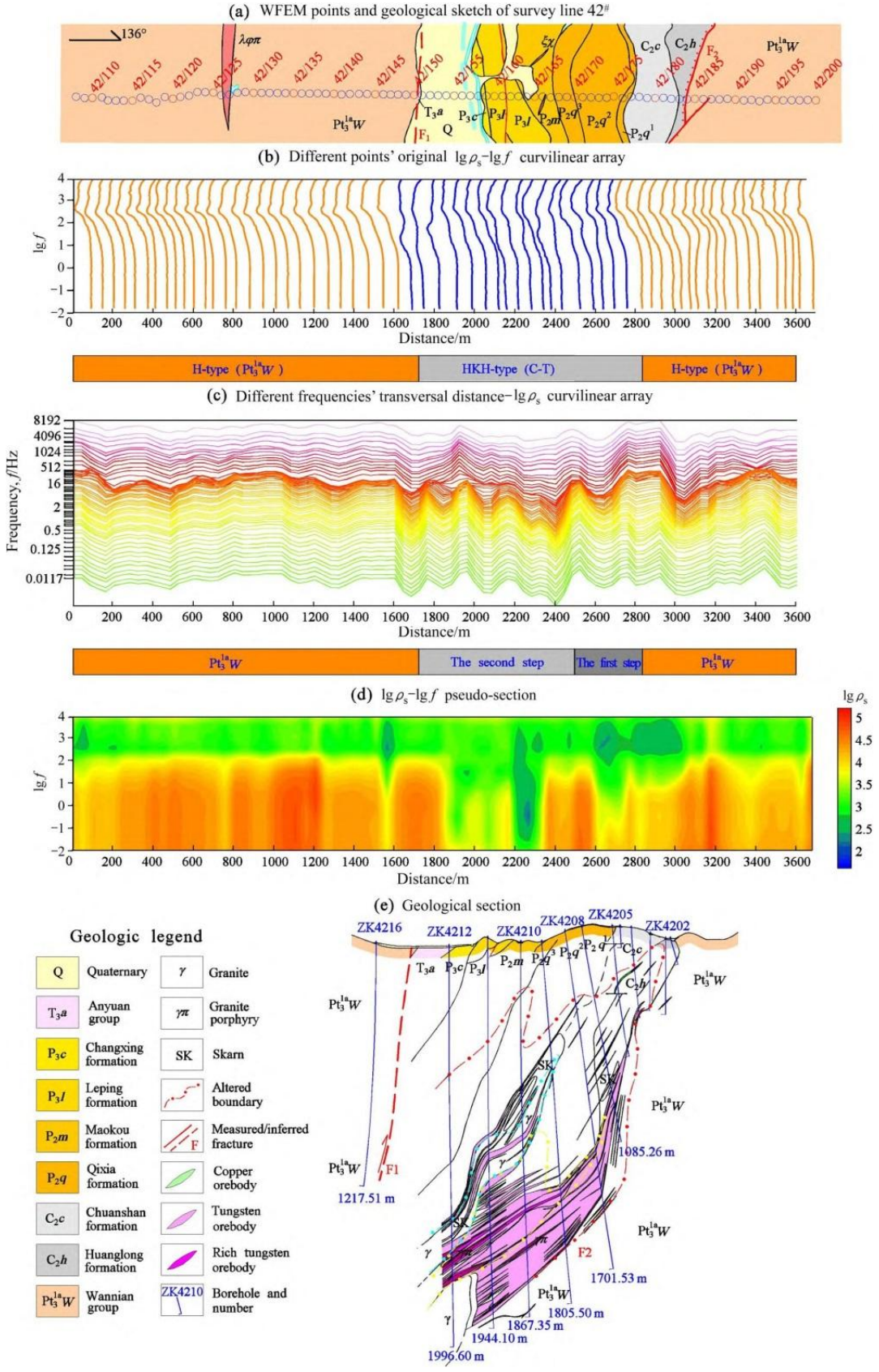

Fig. 4 Qualitative analysis section of Survey Line 42

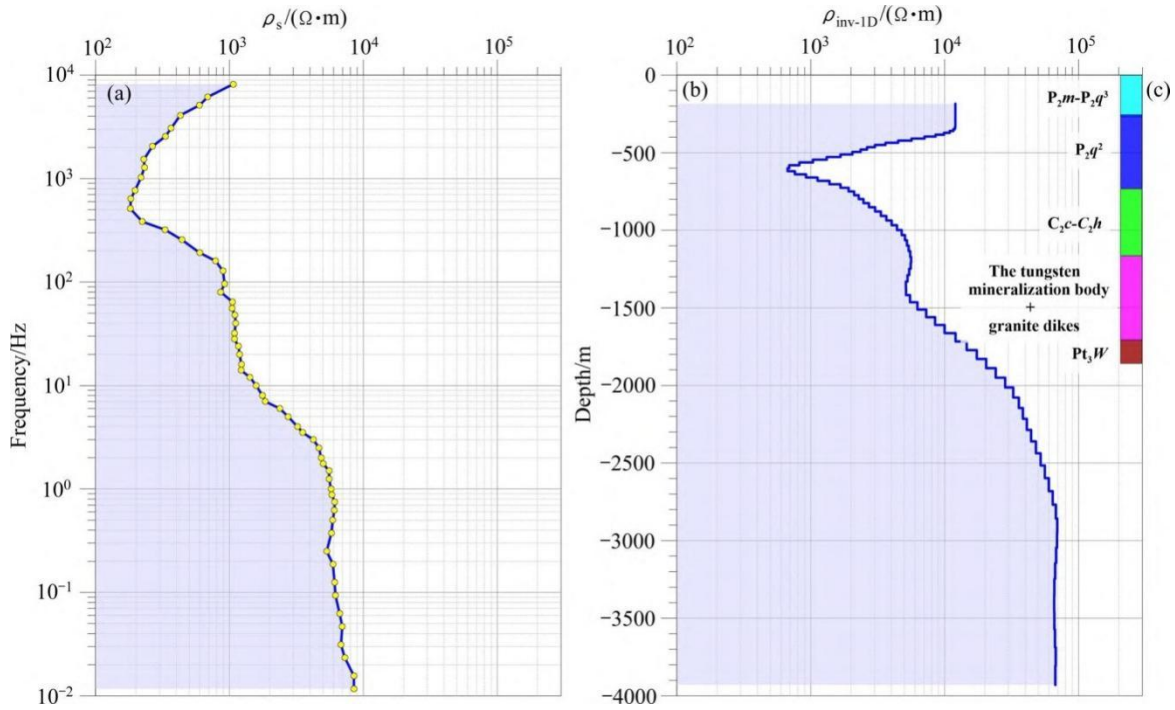

Fig. 5 Wide-field apparent resistivity curve and its 1D inversion nearby Drill ZK4212 on Survey Line 42. (a) Wide-field apparent resistivity curve; (b) 1D inversion result; and (c) simple drill diagram

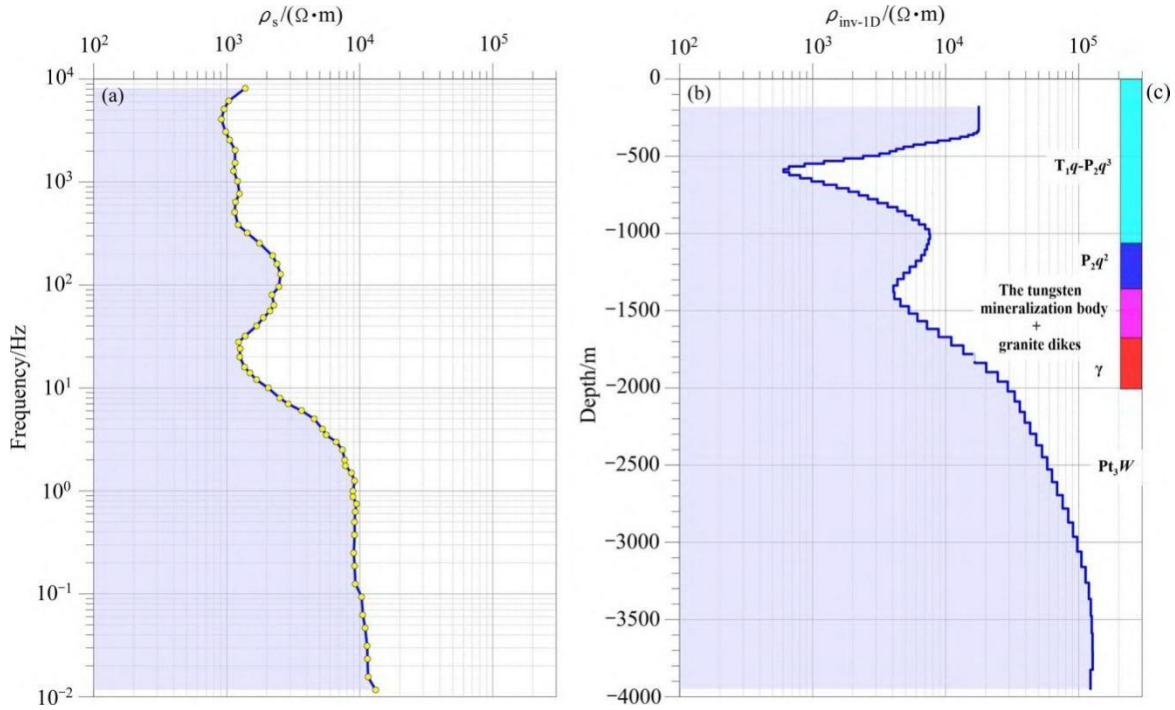

Fig. 6 Wide-field apparent resistivity curve and its 1D inversion nearby Drill ZK4212 on Survey Line 42. (a) Wide-field apparent resistivity curve; (b) 1D inversion result; and (c) simple drill diagram

Calibrated inversion parameters were used to invert the 1D continuum with field sources throughout the area, and the electrical structure of the profile was obtained through a 2.5D continuum inversion of the initial model (Fig. 7(a)). Combined with the physical properties of the above petroformations and electrical data alongside the drill, the area can be divided into four primary electrical layers as follows: (1) P2q1, P2q3, P2m, and P2c are the medium-resistivity layers; (2) the P2q2 limestone layer and intrusion of dikes along the P2/C2 interface are important low-resistivity markers in this area, which can roughly delineate the C_2c and C_2h spaces of the primary ore-bearing horizon with the inferred fault F2 structure; (3) the C_2c and C_2h skarn alteration zones appear as medium-resistivity layers; (4) and $Pt_3^{1a}W$ is the high-resistivity background. Furthermore, the

distortion changed significantly in the middle and shallow sections, and the resistivity increased in the deeper sections.

Extraction of electrical information. Based on the WFEM inversion results (Fig. 7(a)), the background field was extracted (Fig. 7(c)) using the Gaussian low-pass filtering method, and the residual difference between the inversion results and the background field was calculated to obtain the local field (Fig. 7(d)). The background field (Fig. 7(c)) reflects the overall tectonic framework. In contrast, the local field highlights the different lithosets and secondary structures of the Carboniferous Permian strata. Considering Survey Line 42 as an example, separating the background and local fields, the background field shows the transverse segmentation characteristics of the central Carboniferous Permian strata and a shallow metamorphic basement on both sides, which are separated by faults F1 and F2. The $Pt_3^{1a}W$ strata on the north and west sides were overlain with the Carboniferous Permian strata.

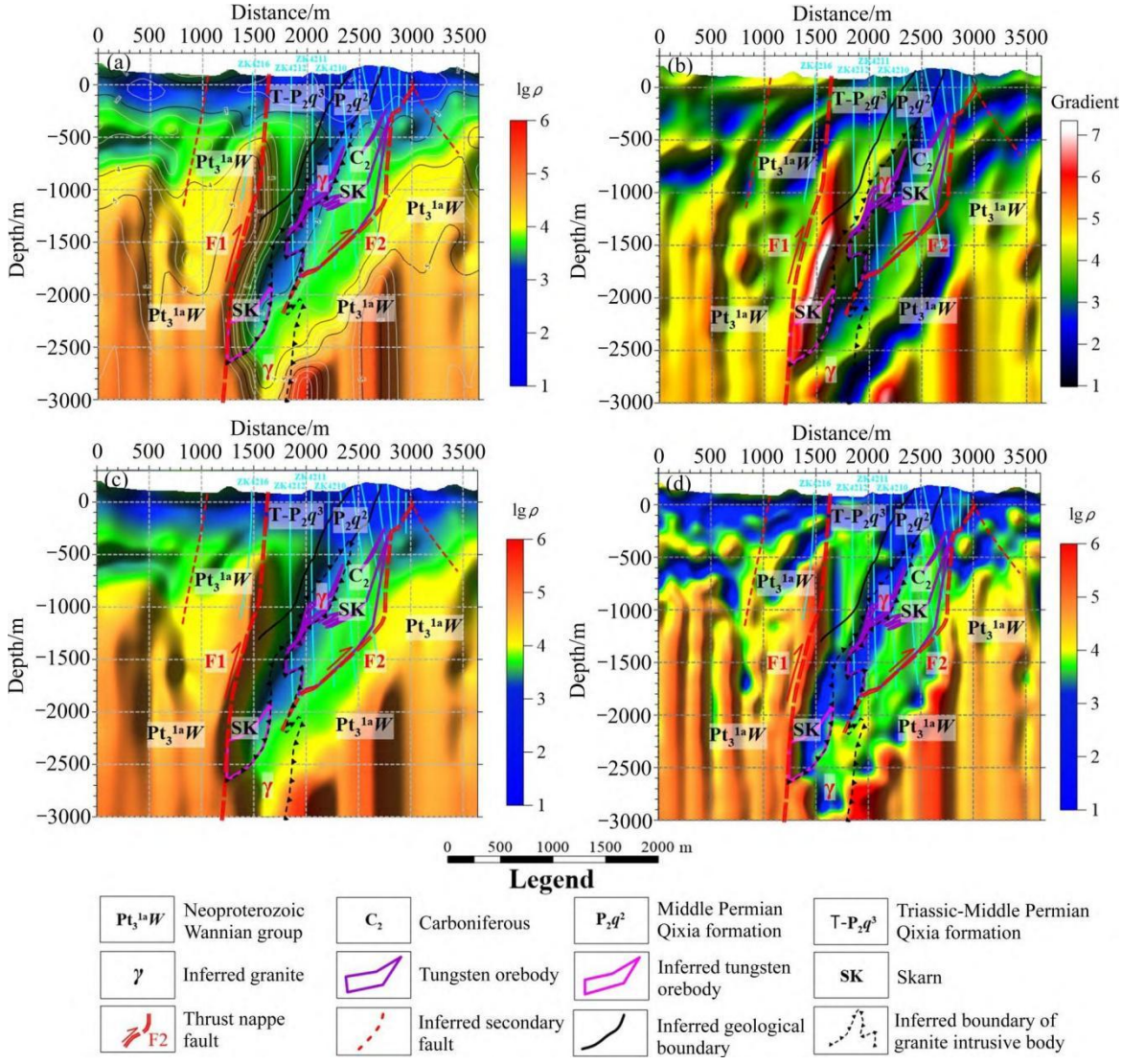

Fig. 7 Background, local resistivity, and resistivity gradient of Survey Line 42. (a) WFEM inversion section; (b) inverse resistivity gradient section; (c) background resistivity; and (d) local resistivity

Boundary enhancement and detection methods, such as derivative and gradient models, were used to identify and determine the fault structure in combination with results from previous studies on mineral deposit structures. The derivative extraction was performed using the Prewitt differential operator. The vertical first (Fig. 8(a)) and second derivatives (Fig. 8(c)) reflect vertical stratification characteristics, whereas the horizontal first (Fig. 8(b)) and second derivatives (Fig. 8(d)) reflect horizontal demarcation characteristics. Simultaneously, based on the vertical second derivative of the inversion results, the analytical signal amplitude (total gradient modulus) was obtained, and edge identification of the fault structure was performed using the maximum position (Fig. 8(b)). Edge identification methods complemented and validated each other. Compared to the first-order

method, the second-order method showed richer details and more evident interfaces. The gradient model was more intuitive for delineating the structural lines and stratification of each rock group. In the section on Survey Line 42, the linear anomaly of the gradient mode described the boundary and location of the ore-controlling faults and nappe structures. The occurrence of fault F1 is extremely steep and locally reversed, whereas that of fault F2 is steep on the upper side and gradual on the lower side. Meanwhile, there was a trend of intersection with fault F1 at greater depths. A series of low-amplitude linear anomalies and dislocations were arranged at certain angles in the shallow metamorphic rock basement on both sides, which were presumed to be secondary structures in the area.

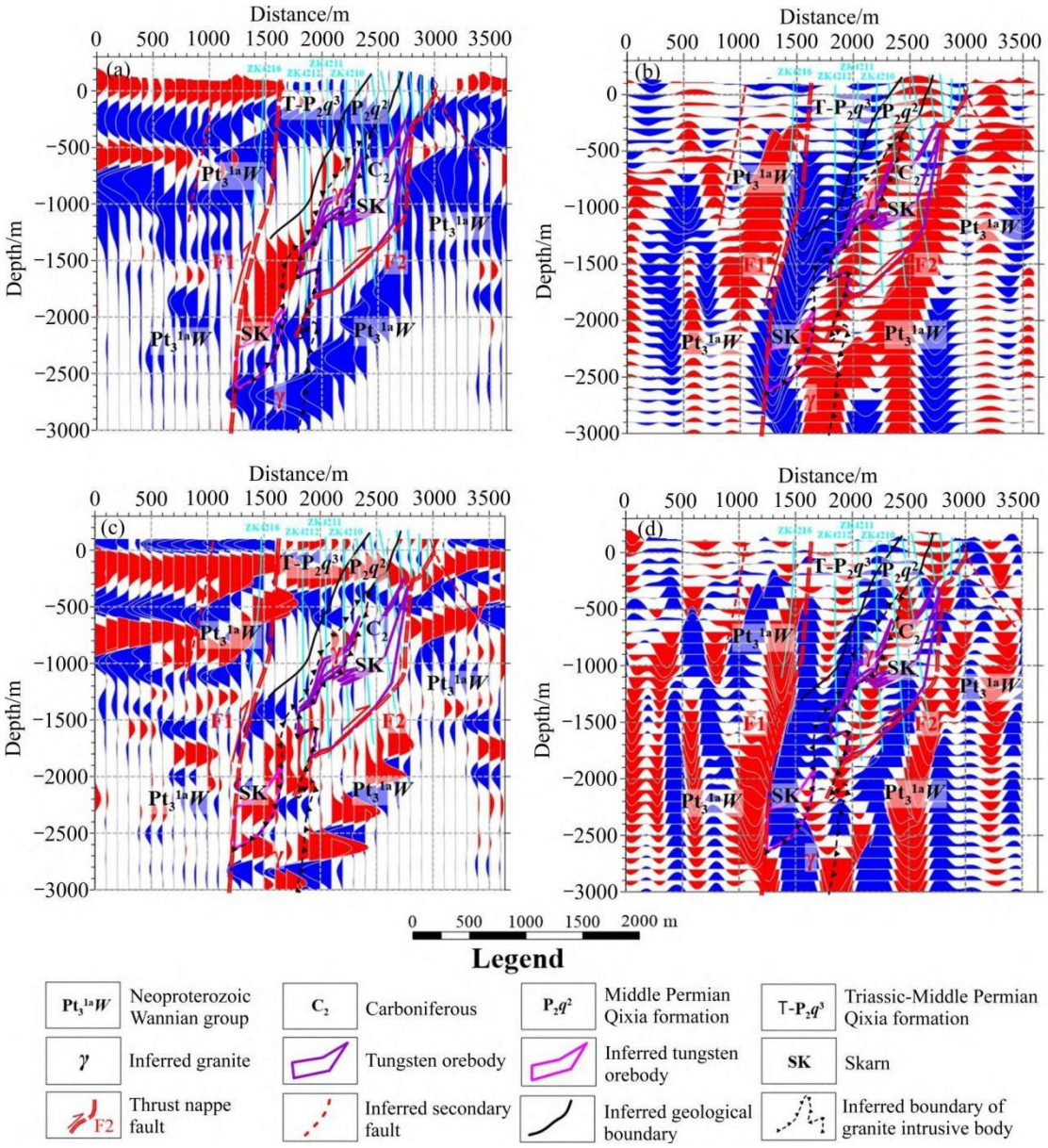

Fig. 8 Derivative calculation of Survey Line 42. (a) Vertical first derivative of ρ; (b) horizontal first derivative of ρ; (c) vertical second derivative of ρ; and (d) horizontal second derivative of ρ

Integrated geological–geophysical interpretation. Multiparameter comprehensive analysis is an effective method for reducing multiple anomaly interpretation solutions. Considering Survey Line 42 as an example, the Bouguer gravity anomaly was low in the middle and gradually increased on both sides (Fig. 9(b)), resulting from the low-gravity anomaly generated by low-density granite and Permian carbonate rocks superimposed on the high-gravity background of the high-density shallow metamorphic rocks and skarn. A high local gravity in a low-gravity area can be considered a sign of a gravity anomaly in the search for skarn-type W–Cu ores. The magnetic anomaly profile (Fig. 9(c)) shows a low distribution of associated positive and negative magnetic anomalies. The △T cascade zone is located near the contact zone between shallow metamorphic and carbonate

rocks and is controlled by fault F2. The inversion results of the 2D apparent magnetic susceptibility imaging (Fig. 9(d)) show an elliptical magnetic source near fault F2, which is abnormally consistent with the high IP value (Fig. 9(e), where n is the apparent polarisability. An analysis of the inversion section of the WFEM (Fig. 9(g)) shows that the electrical gradient interface of the $Pt_3^{1a}W$ shallow metamorphic rock basement is an important marker of the nappe structure. Fault F1 is a compression–torsional thrust nappe structure, and its electrical properties change rapidly in the transverse direction and are steeper in the longitudinal distribution, indicating an extremely steep occurrence and weak hydrothermal alteration activity. Fault F2 is the product of slippage along the weak surface of the structure after thrust and is the primary heat-conducting and ore-controlling structure in this area. Compared to fault F1, fault F2 has a transverse width and a gradual electrical property gradient. Furthermore, it is characterised by a longitudinal stepped form that dips NW and a slower stepped platform, which serves as an important ore-bearing site.

The ore-forming hydrothermal fluid migrated upwards along the primary thermal conduction structure of fault F2, and the upper P_2q Formation and lower $Pt_3^{1a}W$ basement acted as shields. The thick large skarn-type W ore body was formed in the trap in the gradual depression, and the thin vein and mesh fissure-filling Cu ore body was formed in the shallow surface. As the rock mass intrudes upward along fault F2, the alteration products formed by magmatic activity, such as skarn, hornstone, and pyrite, are primarily distributed near fault F2 and exhibit strong magnetic and electrical conductivities, causing local magnetic and geochemical anomalies (Fig. 9(a)).

With increasing depth, faults F1 and F2 show a gradual convergence trend, which restricts the spatial scale of the ore body, resulting in compression of the distribution space of primary ore-bearing horizons C_2c and C_2h.

The buried rock mass was a key geological issue in this study. Hidden rock strains and dikes are often characterised by greater burial depth, smaller scale, complex morphology, and smaller differences in resistivity from the surrounding rock. In addition, it is difficult to identify and locate them based solely on electromagnetic data. As shown in Fig. 10, twisted anomalies with different degrees of relatively low resistivity were observed in the depth range of the orebodies in the four inversion sections, causing a transverse discontinuity in the deeper section. The upper section corresponds to the local low-gravity anomalies and low positively- and negatively associated magnetic anomalies. Currently, several drills have encountered biotite granite, and the rock mass emplacement is distributed at a depth of 1600–2200 m. Due to the density, magnetic, and electrical differences between the rock mass and surrounding rock mass, the combination of gravitational, magnetic, and electrical parameters can be complementary and mutually verified. The "twisted relatively low resistivity anomaly + local low gravity anomaly + low positively- and negatively-associated magnetic anomalies" represents the emplacement of the buried rock mass (Wang et al., 2023; Wei et al., 2023).

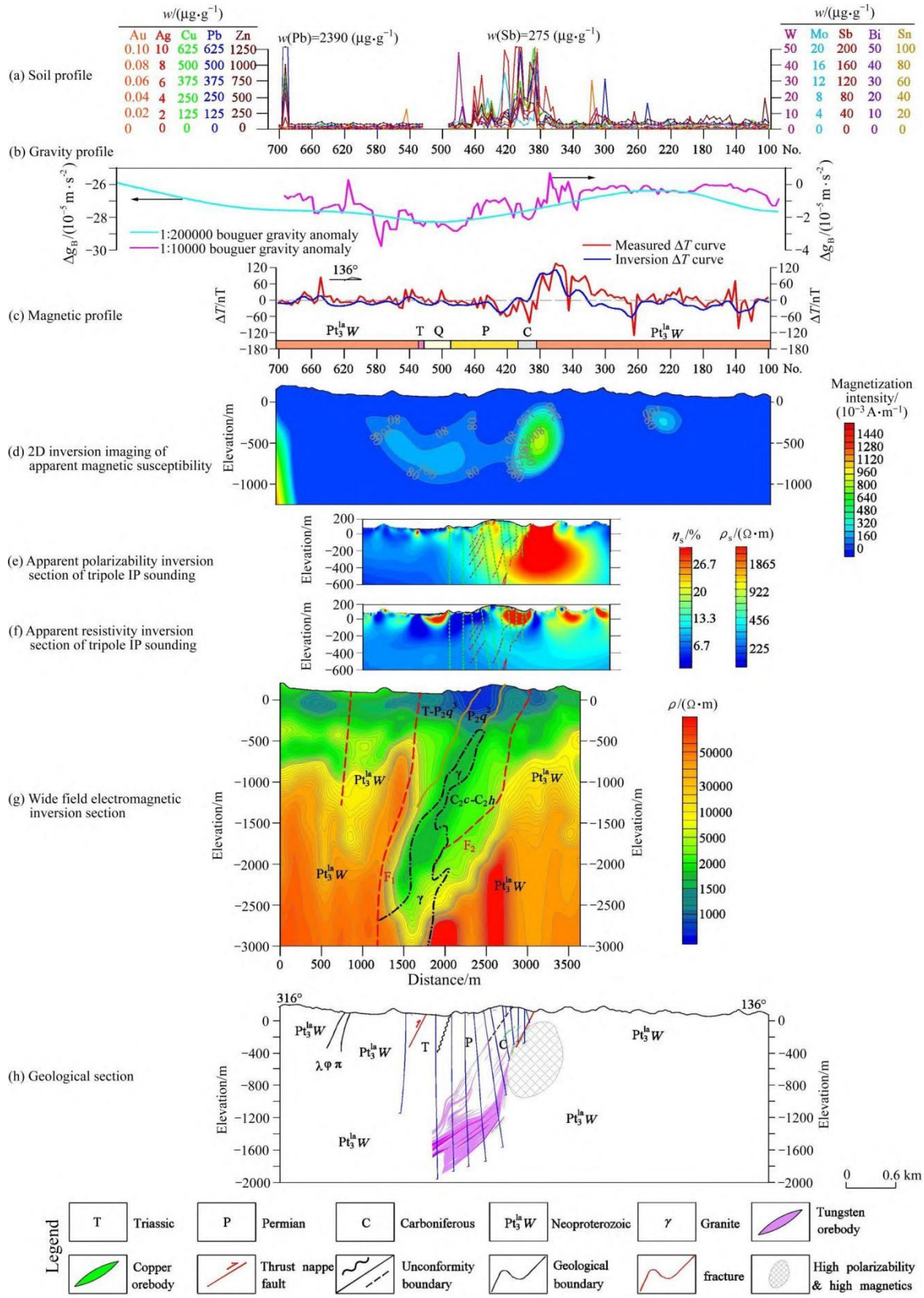

Fig. 9 Geologic and geophysical section of Survey Line 42

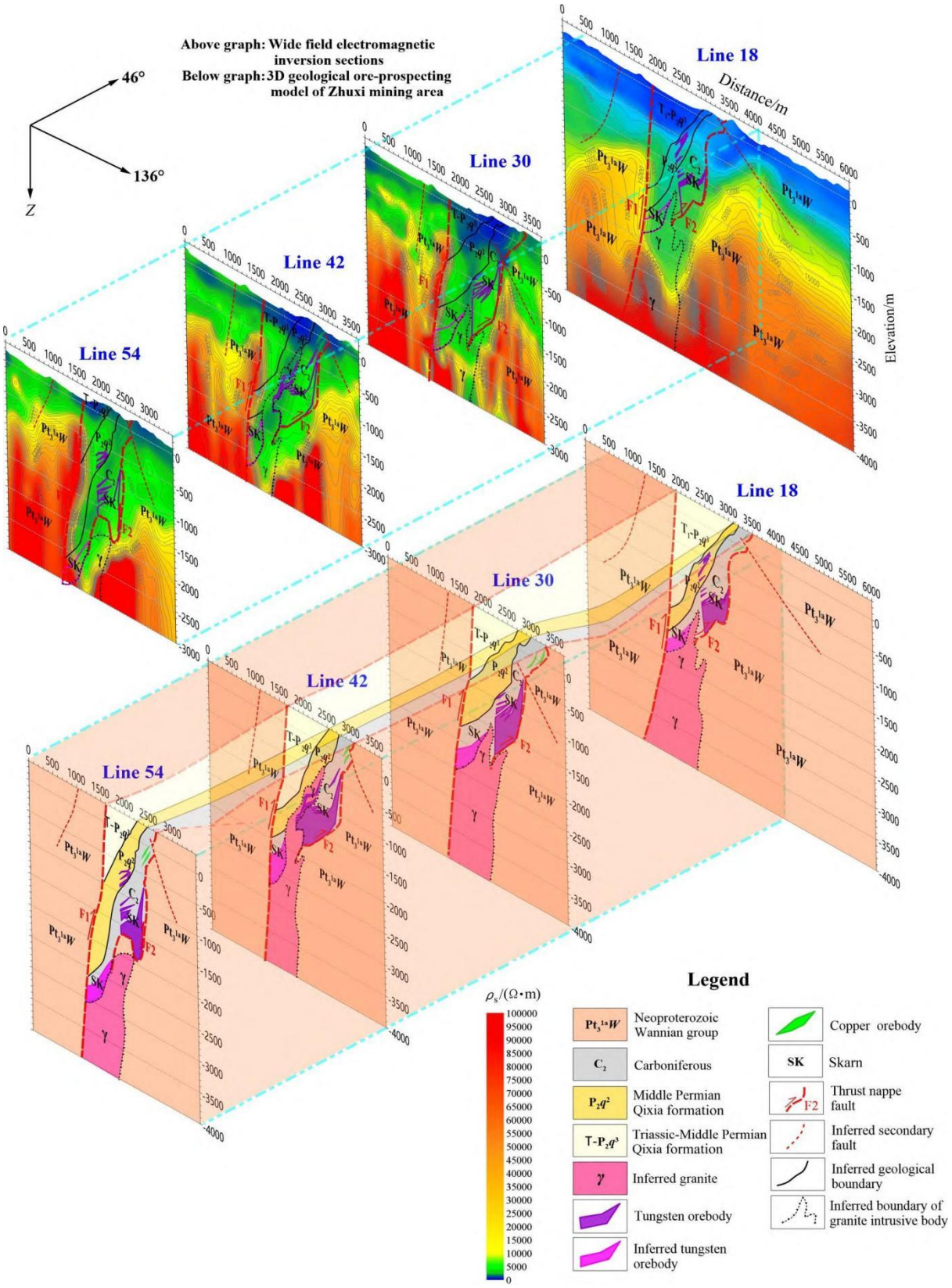

Fig. 10 WFEM inversion sections and 3D geological ore-prospecting model of the Zhuxi area

In summary, the transverse gradient interface of gravity, magnetic, and resistivity mainly reflects the fault tectonic boundary, and high magnetic and high polarisation anomalies indicate magmatic-hydrothermal migration channels. Low gravity anomalies and low, slow-associated positive and negative magnetic anomalies superimposed on the WFEM deeply twisted relatively low resistivity anomalies can extract the emplacement

information of the buried rock mass. The distribution space of the main ore-bearing horizons, C_2c and C_2h, can be roughly delineated by the low-resistance plate marker layer and holding range of the F2 fault in the middle of the section inversion using the WFEM.

Discussion

Metallogenic characteristics. The W–Cu deposit in the Zhuxi area was ore-controlled by a deep thrust fault zone, with ore-bearing performed by a carbonate tectonic sheet and ore formation by a buried rock mass during the late Yanshan (150-133Ma). Based on the WFEM results combined with geological data, a three-dimensional geological prospecting model (Fig. 8) was constructed to reflect the spatial morphology and location relationship of relevant ore-forming geological bodies, and the following two suggestions are proposed for future prospecting: (1) from SE to NW in the area, the W–Cu body inclination gradually decreased, thickness increased, and mineralisation alteration was enhanced. The rocks and dikes were interspersed more frequently, and the hidden rocks demonstrated the potential to form skarn-type W–Cu polymetallic deposits on the NW side and deeper along the dip. (2) Combined with the research results of Ouyang et al. (2018), we can observe that from SW to NE and vertically from bottom to top, metallogenic elements show a trend of W→W–Cu(-Fe)→Cu–W→Cu–Zn→Zn(-Pb–Ag) (from high to low temperature). The emplacement of the rock mass gradually increased; that is, the buried depth of the ore-forming rock mass on the SW side of the Zhuxi area was greater, which should be considered as the next deep prospecting direction. In the future, it is necessary to conduct further research on wide-area electromagnetic data processing and interpretation technologies. For example, the anisotropic inversion of wide-area apparent resistivity (Liu et al., 2018), three-dimensional inversion (Lv et al., 2019), and the joint inversion of wide-area electromagnetic data using data obtained by gravity, magnetic analysis, and other methods (Liu et al., 2019) can be used as future research directions.

Size of the ore body. The mineral resources of the Pingxiang-Leping depression in the Qinhang junction have always been considered to be dominated by coal and nonmetallic minerals, and the scale of the metal deposits is relatively small (Yang et al., 2018). The discovery of the tungsten – copper deposit in Zhuxi introduced the idea of "deep earth" prospecting in the depression zone. The WFEM test results in the Zhuxi tungsten – copper mine show that the method has good spatial positioning for ore body structure, thrust, nappe deep fault, and main ore-bearing horizon and is an effective method for deep metal mineral exploration. The concealed deposits in the Pingxiang-Leping depression have the characteristics of a thick cover, deep burial, large scale, and good preservation, which are advantageous to the implementation of the WFEM in exerting its technical advantages and characteristics.

Conclusions

The following conclusions can be drawn from this study:

(1) The W–Cu deposit in the Zhuxi mining area is among the top three skarn-type W–Cu polymetallic deposits in China. High-quality data were obtained through wide-area electromagnetic sounding tests, and reliable characterisation of deep electrical structures was obtained through processing and interpretation. The two-dimensional geological–geophysical section of Survey Line 42 and the pseudo-three-dimensional map of the wide-area electromagnetic inversion section were used to show the structural framework of the study area and the spatial form, location, and mutual relationship of ore-controlling geological bodies, such as nappe structures, Carboniferous ore-bearing horizons, and hidden rock masses. These data provide a strong basis for studying metallogenic regularity and future prospecting directions at depths of 500 – 3000 m in the Zhuxi mining area.

(2) In this study, the relationships among the electrical properties, density, magnetism, and lithology of the target geological body were established using physical property data and apparent resistivity curves near the drill. Based on reliable original data, quantitative analysis and inversion interpretation were performed, followed by the use of boundary enhancement and recognition methods such as derivative and gradient modes to extract electrical information. Finally, using a combination of gravity, magnetic, and electrical parameters for complementation and verification, a comprehensive geological – geophysical interpretation was conducted, and a three-dimensional characterisation was performed in a quasi-three-dimensional form to construct a three-dimensional geological prospecting model. The acquisition, inversion, and processing of Zhuxi wide-field electromagnetic surveying provided strong support for obtaining quality deep exploration results on the mining area scale and can be applied to deep prospecting for semi-concealed or concealed metal minerals in the Pingle Depression.

References

ANNEN C, BLUNDY JD, SPARKS RSI (2006) The Genesis of Intermediate and Silicic Magmas in Deep Crustal Hot Zones. Journal of Petrology, 47(3): 505-539. https://doi.org/10.1093/petrology/egi084.

CANDELA PA, BOUTON SL (1990) The influence of oxygen fugacity ontungsten and molybdenum partitioning between silicate meltsand ilmenite. Economic Geology 85:633-640. doi: 10.2113/gsecongeo.85.3.633.

CERNÝ P, BLEVIN PL, CUNEY M, LONDON D (2005) Granite-related oredeposits. Econ Geol 100:337-370.

CHEN GH, SHU LS, SHU LY, ZHANG C, OUYANG YP (2015) Geological characteristics and mineralization setting of the Zhuxi tungsten (copper) polymetallic deposit in the eastern Jiangnan Orogen. Scientia Sinia (Terrae) 45(12):1799- 1818, 1-6. doi: 10.12090/j.issn.1006-6616.2018.24.01.002.

CHEN GH, WAN HZ, SHU LS (2012) An analysis on ore-controlling conditions and geological features of the Cu-W polymetallic ore deposit in the Zhuxi area of Jingdezhen, Jiangxi province. Acta Petrologica Sinica 28(12): 3901-3914. http://www.ysxb.ac.cn/en/article/id/aps_20121209.

CHEN GH (2014) The ore-controlling conditions and geological features of the W-Cu polymetallic ore deposit in the Zhuxi area of Jingdezhen, Jiangxi Province. Nanjing: Nanjing University.

DAI SK, WANG SG, ZHANG QJ, XUE DC (2013) 2.5D forward and inversion of CSEM in frequency domain. The Chinese Journal of Nonferrous Metals 23(9): 2513-2523. http://ysxb.csu.edu.cn/previewFile?id=36132095&type=pdf&lang=zh.

GUO X, LAN XY, YAN JY (2020) Large-scale gravity survey and metallogenic prediction: An example of the Zhuxi tungsten deposit in Jiangxi Province. Geology and Exploration 56(5): 985-1004. doi: 10.12134/j.dzykt.2020.05.008.

HART CJ, MAIR JL, GOLDFARB RI, GROVES DI (2004) Source and redoxcontrols on metallogenic variations in intrusion-related ore systems, Tombstone-Tungsten Belt, Yukon Territory, Canada. Transactions of the Royal Society of Edinburgh Earth Sciences 95: 339-356. doi: 10.1017/S0263593300001115.

HE JS (2020) New research progress in theory and application of wide field electromagnetic method. Geophysical and Geochemical Exploration, 2020, 44(5): 985-990. doi: 10.11720/wtyht.2020.0192.

HE JS. Theory and technology of wide field electromagnetic method. The Chinese Journal of Nonferrous Metals, 2019, 29(9): 1809-1816. doi: 10.19476/j.ysxb.1004.0609.2019.09.02.

HE JS (2010) Wide field electromagnetic sounding methods and pseudo-random signal coding electrical method. Beijing: Higher Education Press.

HE JS (2010) Wide field electromagnetic sounding methods. Journal of Central South University (Science and Technology) 41(3): 1065-1072.

HE XL, ZHANG D, CHEN GH, WU GG, HU BJ, HUO HL, LI N, LI F (2018) Genesis of Zhuxi copper-tungsten deposit in Jiangxi Province: Insights from mineralogy and chronology. Journal of Jilin University (Earth Science Edition) 48(4): 1050-1070. doi: 10.13278/j.cnki.jjuese.20170092.

HE XR, CHEN GH, LIU JG, ZHANG C (2011) On the copper-tungsten prospecting orientation in Zhuxi region. China Tungsten Industry 26(1): 9-14. doi: 10.3969/j.issn.1009-0622.2011.01.003.

JUGO PJ (2009) Sulfur content at sulfide saturation in oxidized magmas. Geology 37: 415-418. doi: 10.1017/S0263593300001115.

LI G, HE ZS, TANG T, LIU X, ZHU H (2021) Dictionary learning and shift-invariant sparse coding denoising for contmlled-source electromagneticdata combined with complementary ensemble empirical modedecomposition. Geophysics 86(3): E185-E198, doi: 10.1190/geo2020-0246.1.

LI Y, PAN XF, ZHAO M, CHEN GH，ZHANG TF，LIU X，ZHANG C (2014) LA-ICP-MS zircon U-Pb age, geochemical features and relations to the W-Cu mineralization of granitic porphyry in Zhuxi skarn deposit, Jingdezhen, Jiangxi. Geological Review 60(3): 693-708. https://www.geojournals.cn/georev/georev/article/abstract/20146003020.

LING F, YANG Y, LI G, ZHOU C, HUANG M (2022) Extracting useful high-frequency information from wide-field electromagnetic data using time-domain signal reconstruction. Journal of Central South University 29(11):3767-3778. doi: 10.1007/s11771-022-5180-9.

LIU JG, YANG XP, ZHOU YX, ZENG XH, RAO JF, CHEN GH (2015) Genesis of granites and relationship of mineralization in Zhuxi tungsten-copper deposit, Fuliang County, Jiangxi Province. Resources Survey and Environment 36(4): 276-284. doi: 10.3969/j.issn.1671-4814.2015.04.006.

LIU JX, ZHAO RAN, GUO ZW (2019) Research progress of electromagnetic methods in the exploration of metal deposits. Progress in Geophysics 34(1): 151-160. doi: 10.6038/pg2019CC0222.

LIU SB, WANG CH, LIU ZQ, LIU GJ, YU MC (2014) Northeast Jiangxi Taqian-Fuchun metallogenic belt magmatite time limit and sequence division and its significance. Rock and Mineral Analysis 33(4): 598-611. doi: 10.3969/j.issn.0254-5357.2014.04.023.

LIU YH, YIN CC, CAI J, HUANG W, SUN S (2018) Review on research of electrical anisotropy in electromagnetic prospecting. Chinese Journal of Geophysics 61(8): 3468-3487. doi: 10.6038/cjg2018L0004.

LV QT, ZHANG XP, TANG JT, JIN S, LIANG LZ, NIU JJ (2019) Review on advancement in technology and equipment of geophysical exploration for metallic deposits in China. Chinese Journal of Geophysics 62(10): 3629-3664. doi: 10.6038/cjg2019N0056.

MAO JW, OUYANG HG, SONG SW, SANTOSH M, YUAN SD, ZHOU ZH, ZHENG W, LIU H, LIU P, CHENG YB, CHEN MH (2019) Geology and metallogeny of tungsten and tin deposits in China. Economic Geology 22:411-482.

MAO JW, XIE GQ, DUAN C, PIRAJNO F, ISHIYAMA D, CHEN YC (2011). Atectono-genetic model for porphyry-skarn-stratabound Cu-AuMo-Fe and magnetite-apatite deposits along the Middle-LowerYangtze River Valley, Eastern China. Ore Geology Reviews 43: 294-314.

MEINERT LD, DIPPLE GM, NICOLESCU S (2005) World skarn deposits. Econ Geol 100:299-336.

MENGASON MJ, CANDELA PA, PICCOLI PM (2011) Molybdenum, tungsten and manganese partitioning in the system pyrrhotite-Fe-S-0melt-rhyolite melt: Impact of sulfide segregation on arc magma evolution. Geochimica et Cosmochimica Acta 75:7018-7030. doi: 10.1016/j.gca.2011.08.042

OUYANG YP, CHEN GG, RAO JF (2014) On geological features and metallogenic mechanism of Zhuxi Cu-W polymetallic deposit in Jingdezhen of Jiangxi. Journal of Geology 38(3): 359-364.

OUYANG YP, RAO JF, LIAO SP, WANG SW, LIANG QC, ZHEN DY (2019) Rock- and ore-controlling structure in the Zhuxi ore concentration area in the northeastern Jiangxi Province. Geology in China 46(4): 878-893.

OUYANG YP, RAO JF, YAO ZY, SHU YP, LI JQ, LI Q. Mineralization and prospecting direction of the "Zhuxi type" skarn deposit. Geological Science and Technology Information, 2018, 37(3): 148- 158.

OUYANG YP, ZENG RL, SHU L, M, MIAO ZG, ZHANG TY, HUANG Y (2023) Genesis and geological significance of quartz vein-type wolframite in the deep of Zhuxi W-Cu deposit. Journal of Guilin University of Technology 43(2):184-192.

RICHARDS JP. (2011). Magmatic to hydrothermal metal fluxes in conver-gent and collided margins. Ore Geology Reviews 40:1-26.

SCHMIDT C, ROMER RL, WOHLGEMUTHR CC, APPELT O (2020) Partitioning of Sn and W between granitic melt andaqueous fuid. Ore Geology Reviews, 117:103263. doi: 10.1016/j.oregeorev.2019.103263.

WAN HZ, LIU ZQ, LIU SB (2015) LA- ICP-MS zircon U-Pb dating of granodioritic porphyry located Zhuxi copper-tungsten mine in northeast Jiangxi and its geological significance. Rock and Mineral Analysis 34(4): 494-502.

WANG XG, HU ZH, CHEN GH, ZHEN DY, YIN XK, LI SY (2021) Application of Zhuxi-style "vein-lay-contact ore body" prospecting method near existing deposit to deep mineral exploration. China Tungsten Industry 35(5): 1-9.

WANG XG (2020) The prospecting obvious breakthrough and technological innovation of Jiangxi Geological Exploration Fund. Nanchang: Jiangxi Science and Technology Press.

WEI XL (2016) New discoveries of tungsten ore prospecting in China. China Tungsten Industry 31(3): 1-7.

WU XP, OUYANG YP, ZHOU YX (2015) Geochemical characteristics of magmatite and their constraints on mineralization of the Zhuxi tungsten-copper polymetallic deposit in Jingdezhen, Jiangxi Province. Geology in China 42(6): 1885- 1896.

XIA ZZ, WANG XG (2016) Metallogenic and diagenic mechanism of the detachment and nappe orogenesis at the Zhuxi super-large tungsten-copper deposit in Jiangxi Province. Journal of Geology 40(4): 552-559. doi: 10.3969/j.issn.1674-3636.2016.04.552.

XIE T, FENG Y, LUO LC, SHI BD, YANG B, SHAN SX (2015) Study on ore- controlling characteristics of Zhuxi W-Cu deposit in Jingdezhen, Jiangxi Province. Acta Mineralogica Sinica 35(S1): 79-80.

YAN TJ (2017) Comprehensive study of geophysical methods to the deep prospecting of tungsten-copper ploymetallic ore in Zhuxi area of Jiangxi. Changchun: Jilin University.

YANG M, MEI Y (1997) Characteristics of geology and metallization in the Qinzhou-Hangzhou paleoplate juncture. Geology and Mineral Resources of South China 13(3): 52-59.

YANG MG, YU ZZ, TANG WX, GE QY, ZHI QQ, WU JN (2018) On strategy for deep prospecting. Shanghai Land & Resources 39(4): 65-74.

ZHANG S, ZHANG N, WU HY, ZENG Y, ZHANG ZX (2018) Application of low-altitude aeromagnetic technology in Zhuxi mining area of Jiangxi. Global Geology 37(2): 595-601. doi: 10.3969 / j.issn.1004-5589.2018.02.026.